research papers

On qualitative and quantitative analysis in analyser-based imaging

Ya. I. Nesterets,[a]* P. Coan,[b] T. E. Gureyev,[a] A. Bravin,[b] P. Cloetens[b] and S. W. Wilkins[a]

[a]CSIRO Manufacturing and Infrastructure Technology, PB 33, Clayton South, Victoria 3169, Australia, and [b]European Synchrotron Radiation Facility, BP 220, 38043 Grenoble CEDEX, France. Correspondence e-mail: yakov.nesterets@csiro.au

Using rigorous wave-optical formalism, a general expression is obtained for the image intensity distribution in combined analyser-based/propagation-based phase-contrast imaging. This expression takes into account partial coherence of the wave incident on the object as well as the finite resolution of the detector system. Using this general expression, two approaches based on the geometrical optics and weak-object approximations are applied to derive simple solutions to the inverse problem of reconstruction of the phase and amplitude of the object wave. With the help of numerical experiments, the two approaches are compared in terms of their validity conditions and are shown to impose certain restrictions on the properties of the object wave. In particular, it is shown that violation of the validity conditions of the geometrical optics or weak-object approximations results in the appearance of strong reconstruction artefacts in the transmitted intensity near the edges of the objects. The effect of the incident wavefront non-uniformity due to imperfections of the imaging set-up on image formation and phase/amplitude reconstruction is also discussed. A solution to this problem is proposed in the form of a multi-image phase/amplitude reconstruction algorithm based on the geometrical optics approximation. This algorithm and an algorithm based on the weak-object approximation are applied to simulated and experimental images of fibres.

1. Introduction

In recent years, a number of X-ray phase-contrast imaging methods have been developed using laboratory sources and synchrotrons (Fitzgerald, 2000). The success of these imaging methods can be explained by the fact that for objects consisting of low-Z elements and for high X-ray energies the attenuation properties of the objects are almost uniform, which results in a very weak contrast in conventional absorption images. At the same time, the phase modulations of the wave transmitted through the objects are several orders of magnitude larger compared with the attenuation modulations and can potentially produce a relatively high contrast in the images if an appropriate phase-sensitive optical configuration is used. One such optical configuration (called analyser-based imaging, or ABI) utilizes a perfect flat crystal placed after the object (Förster et al., 1980; Somenkov et al., 1991; Ingal et al., 1994, 1995; Ingal & Beliaevskaya, 1995; Davis et al., 1995a,b). The phase modulations induced by the object cause small (of the order of a microradian) local deviations of the propagation direction of the wave transmitted through the object. The analyser crystal, whose reflectivity curve has typical FWHM of the order of several microradians, is very sensitive to these small deviations of the object wave. The diffraction of the object wave in the analyser crystal results in spatial modulation of the reflected intensity. These spatial intensity modulations are registered in the image plane by a position-sensitive detector.

The spatial intensity modulations in the images obtained in the ABI regime differ from the spatial modulations of the phase in the object wave. In general, the relationship between those two is quite complicated and the images do not directly resemble the phase distribution. In order to obtain the phase distribution in the object wave, an appropriate processing of the collected images is necessary. This phase reconstruction procedure presents an example of the inverse problem that is non-trivial and hard to solve in the general case. However, using some *a priori* information about the object (for example, characteristic length scale and magnitude of the modulations of refractive index), the relationship between the image intensity and phase distribution can be simplified allowing one to solve the reconstruction problem using an appropriate algorithm.

Most of the algorithms developed so far for the extraction of the phase and amplitude information of the object wave from the analyser-based phase-contrast images (see, for

example, Chapman *et al.*, 1997; Bushuev & Sergeev, 1999; Bushuev *et al.*, 2002; Oltulu *et al.*, 2003; Pagot *et al.*, 2003; Rigon *et al.*, 2003; Wernick *et al.*, 2003) are based on the geometrical optics approximation, which relates in a simple way the intensity $I_h(x, y)$ of the wave reflected by the analyser crystal, characterized by the rocking curve $R(\omega)$, with the phase derivative $\partial_x\varphi(x, y)$ and intensity $I_0(x, y)$ of the wave incident on the analyser crystal (Indenbom & Chukhovskii, 1972; Bushuev *et al.*, 1996, 1998; Gureyev & Wilkins, 1997),

$$I_h(-x, y; \omega) \cong I_0(x, y)R(\omega + k^{-1}\partial_x\varphi(x, y)),$$

where k is the wavenumber. This approximation is valid if the phase of the wave incident on the analyser crystal is a slowly varying function on the length scale of the extinction length of the analyser crystal (Gureyev & Wilkins, 1997; Bushuev *et al.*, 1998). A similar criterion was obtained by Pavlov *et al.* (2004) for the case of a monochromatic plane wave incident on the object. By analogy with the case of propagation-based imaging (where the geometrical optics approximation is valid for large Fresnel numbers), the criterion was formulated as the requirement for large values of the Takagi number,

$$N_T = (h/\lambda)^2 |r(\omega)/r''(\omega)|,$$

where $r(\omega)$ is the analyser's amplitude reflection coefficient as a function of the angular deviation ω of the angle of incidence from the exact Bragg angle, λ is the X-ray wavelength and h is the size of the smallest feature in the object, or the resolution limit of the imaging system, whichever is larger. Condition $N_T \gg 1$ is usually violated at the edges of strong phase objects where the curvature of the induced phase is large, and this results in poor reconstruction of the phase. As we show in the present paper, this factor has to be taken into account when methods based on the geometrical optics approximation are used for the phase/amplitude reconstruction.

Phase/amplitude reconstruction in ABI is significantly complicated by the fact that the wave incident onto the object is usually non-flat. This non-flatness originates from the optical elements of the imaging beamline due to: (i) non-uniformity of the thickness of the X-ray filters and beryllium windows; (ii) deformations of the monochromator crystals due to significant heat load and gravitation; (iii) use of bent crystals and mirrors in monochromators (*e.g.* in the Laue geometry in order to enlarge the bandpass) and focusing optics. Additional wavefront distortions can also occur due to aberrations of the optical elements placed after the object, for example, the analyser crystal and the X-ray/visible-light convertors in the detecting systems. The transverse distribution of the intensity in the wave incident on the object is also non-uniform, mainly due to the angular inhomogeneity of the radiation of the relativistic electrons in the storage ring. These two factors result, in particular, in the non-uniform flat-field images (*i.e.* images collected without an object). Moreover, correction of the images of the object for the incident wavefront curvature cannot be performed by a simple division of the images by the corresponding flat-field images. This is because the non-flatness of the incident wavefront effectively means that different parts of the image correspond to different

deviations of the analyser crystal from the exact Bragg angle even if we assume the analyser crystal to be ideally flat and homogeneous.

In recent years, attempts have been made to separate various contrast mechanisms in the ABI. These mechanisms include refraction contrast arising due to the phase modulation of the wave transmitted through an object, absorption contrast due to attenuation of the X-rays in the object and the so-called 'extinction' contrast, which is just a result of the filtering properties of the analyser crystal, which does not reflect X-rays incident on the analyser at the angles outside its narrow reflectivity curve. It is worth mentioning that the idea proposed by Ingal *et al.* (1994, 1995) regarding the use of a pair of images collected at opposite slopes of the rocking curve of the analyser crystal for producing new images was later successfully implemented in the diffraction-enhanced imaging (DEI) algorithm by Chapman and co-workers (Chapman *et al.*, 1997). This algorithm allows one to separate refraction contrast from the sum of absorption and 'extinction' contrasts. A lot of effort has been undertaken subsequently in order to separate the true absorption from the 'extinction' contrast. The latter is usually attributed to the small-angle X-ray scattering (SAXS) at the sharp edges of the features present in the object. Several approaches have been suggested to this end, two of which, multiple-image radiography (MIR) (Wernick *et al.*, 2003) and an approach suggested by Pagot *et al.* (2003), are very similar in their experimental implementations, involving the measurement of a series of images corresponding to different deviation angles of the analyser covering its rocking curve, but differ in the subsequent analysis of the images. The main idea of the MIR approach consists of computation of multiple parametric images of the object from multiple acquired images. These parametric images are calculated from the deconvolved angular distributions of the scattered intensity in each pixel of the object and include the integrated intensity, the refraction angle and the width of the SAXS intensity distribution. The same parametric images as well as the 'maximum absorption' one are calculated by Pagot *et al.* (2003) by a simple calculation of the moments of the angular distributions of the intensity at each pixel in the image plane. Another approach to the solution of the same problem of separating absorption contrast from ultra-small-angle scattering has been formulated by Rigon *et al.* (2003) and consists of the measurement of two images corresponding respectively to the top and one of the tails of the rocking curve. We should emphasize here that all these methods are based on the geometric optics approximation and therefore are restricted to the objects satisfying the condition $N_T \gg 1$ (Pavlov *et al.*, 2004).

The present paper is arranged as follows. In §2, we derive a general expression for the intensity distribution in the images obtained in the combined analyser-based/propagation-based phase-contrast imaging using a finite spatially incoherent polychromatic X-ray source and finite resolution detector. This general expression is then simplified by using two approaches, based respectively on the geometrical optics approximation and on the weak-phase-object approximation.

research papers

The validity conditions for the two approximations are also obtained. These two approaches are compared in §3 using numerical simulation of the ABI images of simple test objects (cylinders) and reconstruction of the phase of the object wave from these images. §4 is dedicated to the introduction of a new multi-image phase/amplitude reconstruction technique based on the geometrical optics approximation. This approach is applied to both the simulated and the experimental images of fibres. Conditions of applicability of this method are also discussed.

2. General formalism

2.1. General expression for quasi-monochromatic analyser-based/propagation-based phase-contrast imaging

We perform analysis of the ABI for the imaging configuration presented in Fig. 1, consisting of a polychromatic X-ray source (S), a double-crystal monochromator (M), an object (O), a single-crystal analyser (A) and a detector (D). We consider the case of symmetric reflections in all three crystals. In this case, the complex amplitude E_D of the wave created by a monochromatic point source located at a point x_0 of the source plane is expressed in the detector plane *via* transmission function $q(x)$ of the object and point-spread functions of the imaging set-up before and after the object, $G_b(x)$ and $G_a(x)$, respectively, as follows (Nesterets *et al.*, 2005):

$$E_D(-x; x_0, \lambda) = \int_{-\infty}^{+\infty} dx'\, G_b(x' - x_0) q(x') G_a(x - x'). \quad (1)$$

We restrict our consideration to the one-dimensional case. Generalization to the two-dimensional case is straightforward. Equation (1) can be presented in the equivalent form

$$E_D(-x; x_0, \lambda) = \int_{-\infty}^{+\infty} \int_{-\infty}^{+\infty} dudU \exp(2\pi i u x_0) \exp[-2\pi i(u + U)x]$$
$$\times \hat{G}_b(u)\hat{q}(U)\hat{G}_a(u + U), \quad (2)$$

where hereafter $\hat{f}(u)$ denotes the Fourier transform of the function $f(x)$, $\hat{f}(u) \equiv \int_{-\infty}^{+\infty} dx \exp(2\pi i u x) f(x)$. The transfer functions of the imaging set-up before and after the object have the following form (Nesterets *et al.*, 2005):
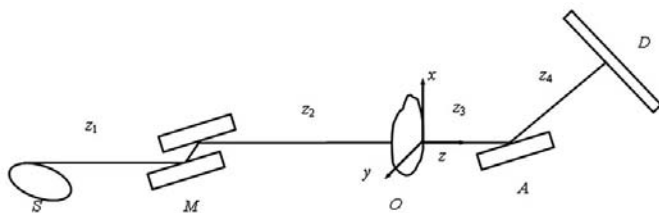

Figure 1
Schematic representation of the analyser-based/propagation-based phase-contrast imaging set-up used in the paper. S X-ray source, M double-crystal monochromator, O object, A single-crystal analyser and D detector.

$$\hat{G}_b(u) = \exp(-i\pi\lambda z_{12}u^2) r_1(\omega_1 - \lambda u) r_2(\omega_2 - \lambda u),$$
$$\hat{G}_a(u) = \exp(-i\pi\lambda z_{34}u^2) r_3(\omega_3 - \lambda u), \quad (3)$$

where r_i denotes the amplitude reflection coefficient of the ith crystal and ω_i is the angular deviation of the ith crystal from the exact Bragg angle, $z_{12} = z_1 + z_2$ and $z_{34} = z_3 + z_4$ are the source-to-object and object-to-detector distance, respectively.

We are interested in the expression for the intensity in the image plane that takes into account the spectral and spatial intensity distribution of the source expressed by the intensity distribution function $S(x, \lambda)$ and the detector's resolution expressed by the point spread function $D(x)$. As in our earlier paper (Nesterets *et al.*, 2005), we shall assume that the spectral distribution is the same for all points of the source (so that the intensity distribution function S can be factorized into the spatial and spectral intensity distribution functions) and the spectral interval that makes a contribution to the resultant image is very small, $[\lambda - \lambda_0]/\lambda_0$ is of the order of 10^{-3} or smaller, so that:

1. the intensity distribution function of the source is almost wavelength independent within this spectral interval (in the vicinity of an average wavelength λ_0) and can be written as $S(x, \lambda_0)$;

2. the object transmission function can be considered wavelength independent and calculated at the average wavelength λ_0 (thus anomalous-dispersion effects near absorption edges are excluded from further consideration);

3. free-space propagation can be considered wavelength independent and calculated at the average wavelength λ_0;

4. dispersion formula $r(\omega; \lambda) \simeq r(\omega - [\lambda - \lambda_0]/\lambda_0 \tan \theta_B; \lambda_0)$ (see, for example, Pinsker, 1978; Nesterets *et al.*, 2005) can be used for the crystals (it is assumed that the whole spectral interval contributing to the resultant image is far from the absorption edges of the material of the crystals).

Under the conditions formulated above, calculations similar to those in Nesterets *et al.* (2005) result in the following expression for the intensity distribution in the image plane, integrated over the wavelength and source size and convolved with the detector point-spread function (PSF),

$$I_D(-Mx) \cong \int_{-\infty}^{+\infty} \int_{-\infty}^{+\infty} dUdV \exp[-2\pi i(U - V)x] \hat{q}(U) \hat{q}^*(V)$$
$$\times \hat{G}(U, V), \quad (4)$$

where we have introduced the transfer function of the imaging system,

$$\hat{G}(U, V) = z_{tot}^{-1} \hat{S}(-[1 - (1/M)][U - V], \lambda_0) \hat{D}([U - V]/M)$$
$$\times \exp[-i\pi\lambda_0 z'(U^2 - V^2)]$$
$$\times Q(-[1 - (1/M)][U - V], U, V), \quad (5)$$

and the transfer function of the monochromator–analyser subsystem,

$$Q(u, U, V) = \cot \theta_B \int\limits_{-\infty}^{+\infty} d\xi \, r_1(\omega_1 + \xi - \lambda_0 u) r_2(\omega_2 + \xi - \lambda_0 u)$$
$$\times r_3(\omega_3 + \xi - \lambda_0 u - \lambda_0 U) r_1^*(\omega_1 + \xi)$$
$$\times r_2^*(\omega_2 + \xi) r_3^*(\omega_3 + \xi - \lambda_0 V). \quad (6)$$

Here $z_{tot} = z_{12} + z_{34}$ is the total source-to-detector distance, $M = z_{tot}/z_{12}$ is the magnification and $z' = z_{34}/M$ is the effective object-to-detector free-space propagation distance.

We should emphasize that so far we have not imposed any restrictions on the object transmission function (except for the wavelength independence). Equation (4) presents a solution of the direct problem of finding the intensity distribution in the images if an object transmission function is known. Inversion of this equation with respect to the object transmission function is not trivial and cannot in general be presented in a simple analytical form. In order to proceed further and simplify equation (4), some assumptions regarding the object transmission function (or the system transfer function) have to be made.

2.2. Geometrical optics approximation and its validity conditions

Let the transmission function of the object vary slowly compared to the point spread function $G(x)$ of the imaging system (the corresponding width of the Fourier transform of the former is small compared to the characteristic length scale of the variations of the system transfer function) so that the transfer function of the imaging system can be approximated by the following finite Taylor series:

$$\hat{G}(U, V) \approx \hat{G}(0, 0) + U \partial_U \hat{G}(0, 0) + V \partial_V \hat{G}(0, 0)$$
$$+ \tfrac{1}{2} U^2 \partial_{UU}^2 \hat{G}(0, 0) + UV \partial_{UV}^2 \hat{G}(0, 0)$$
$$+ \tfrac{1}{2} V^2 \partial_{VV}^2 \hat{G}(0, 0). \quad (7)$$

Before proceeding further, we make additional simplifying assumptions. First, we shall assume that the source-to-object distance z_{12} is much larger than the object-to-detector distance z_{34} so that magnification is close to unity, $M = 1$, which means that a plane wave is incident on the object. Second, we shall assume the detector to be perfect (with δ-function-like resolution). These assumptions lead to the following expression for the transfer function of the imaging system:

$$\hat{G}(U, V) \cong z_{tot}^{-1} S(\lambda_0) \exp[-i\pi \lambda_0 z_{34}(U^2 - V^2)] Q(0, U, V), \quad (8)$$

where $S(\lambda_0)$ now represents the total intensity of the source at wavelength λ_0.

Substituting equations (7) and (8) into equation (4) and neglecting the terms proportional to the second and higher powers of k^{-1}, the following result for the intensity in the image plane is obtained:

$$I_D(-x) \cong I_0(x) R(\omega_1, \omega_2, \omega_3 + k^{-1} \varphi'(x))$$
$$\times \left\{ 1 - k^{-1} z_{34} [\varphi''(x) + \varphi'(x) I_0'(x)/I_0(x)] \right.$$
$$\left. + k^{-1} I_0'(x)/I_0(x) \frac{R_1(\omega_1, \omega_2, \omega_3 + k^{-1} \varphi'(x))}{R(\omega_1, \omega_2, \omega_3 + k^{-1} \varphi'(x))} \right\}, \quad (9)$$

where $I_0(x)$ and $\varphi(x)$ are the intensity and the phase of the wave incident on the analyser,

$$R(\omega_1, \omega_2, \omega_3) = \cot \theta_B \int\limits_{-\infty}^{+\infty} d\xi \, |r_1(\omega_1 + \xi) r_2(\omega_2 + \xi) r_3(\omega_3 + \xi)|^2$$

is the integral reflectivity of the monochromator–analyser subsystem and

$$R_1(\omega_1, \omega_2, \omega_3) = \cot \theta_B \int\limits_{-\infty}^{+\infty} d\xi \, |r_1(\omega_1 + \xi) r_2(\omega_2 + \xi)|^2$$
$$\times \text{Im}\{r_3'(\omega_3 + \xi) r_3^*(\omega_3 + \xi)\}.$$

This result closely resembles equation (8) in Pavlov et al. (2004) but unlike the latter, which has been obtained under the assumption of a monochromatic plane wave incident on the object, equation (9) is valid for the incident quasimonochromatic plane wave. In the case of negligibly small object-to-detector distance z_{34} and weakly absorbing object, the second and the third terms in the curly brackets of equation (9) can be omitted,

$$I_D(-x) \cong I_0(x) R(\omega_1, \omega_2, \omega_3 + k^{-1} \varphi'(x)). \quad (10)$$

Equation (10) has the well known form of the geometrical optics (GO) approximation obtained (Bushuev et al., 1996, 1998; Gureyev & Wilkins, 1997) for a plane monochromatic incident wave. To the best of our knowledge, equation (10) for the analyser-based image intensity in the GO approximation in the case of a quasimonochromatic incident wave has not been previously rigorously derived, although it was used in a number of published experimental works. We apply this equation later in the paper for solution of the ABI phase-retrieval problem.

We now turn our attention to the formulation of the validity conditions. It was suggested by Pavlov et al. (2004) that the validity condition for the geometrical optics approximation can be formulated as the requirement for the Takagi number to be large, $N_T \gg 1$. In the case of a monochromatic plane wave incident on the object, the Takagi number has the following simple form (Pavlov et al., 2004): $N_T = (h/\lambda)^2 |r(\omega)/r''(\omega)|$. In the case of a quasimonochromatic plane wave incident on the object, the corresponding validity condition for the geometrical optics approximation can be written as follows:

$$(2\pi)^2 \hat{G}(0, 0) \max^{-1} \left\{ \left| \partial_{UU}^2 \hat{G}(U, V) \right|_{\substack{U=0 \\ V=0}} \max_x \left| \frac{q''(x)}{q(x)} \right|, \right.$$
$$\left. \left| \partial_{UV}^2 \hat{G}(U, V) \right|_{\substack{U=0 \\ V=0}} \max_x \left| \frac{q'(x)}{q(x)} \right|^2 \right\} \gg 1. \quad (11)$$

Inequality (11) can be interpreted as a simultaneous restriction on the curvature of the transfer function of the imaging

set-up and on the smoothness of the object transmission function.

2.3. 'Weak-object' approximation

In order to proceed further, we present equation (4) in the following equivalent form:

$$I_D(-Mx) \cong \int\limits_{-\infty}^{+\infty} \int\limits_{-\infty}^{+\infty} \mathrm{d}X \mathrm{d}Y \, q(x-X)q^*(x-Y)G(X,Y), \quad (12)$$

where

$$G(X,Y) \equiv \int\limits_{-\infty}^{+\infty} \int\limits_{-\infty}^{+\infty} \mathrm{d}U \mathrm{d}V \exp[-2\pi i(UX-VY)]\hat{G}(U,V). \quad (13)$$

The object complex transmission function $q(x)$ can be expressed *via* the real phase function $\varphi(x)$ and attenuation function $\mu(x)$ as follows:

$$q(x) \equiv \exp[i\varphi(x) - \mu(x)]. \quad (14)$$

Assuming that the attenuation due to the object is weak, *i.e.* $|\mu(x)| \ll 1$, and that the phase is either weak or slowly varying on the characteristic length scale of the system (PSF, G), the product of the two shifted object transmission functions in equation (12) can be presented in the following form:

$$q(x-X)q^*(x-Y) \cong 1 + i\{\varphi(x-X) - \varphi(x-Y)\} - \mu(x-X) - \mu(x-Y).$$

This expansion results in the following solution for the Fourier transform of the intensity distribution in the image plane (see Nesterets *et al.*, 2005, for details):

$$M^{-1}\hat{I}_D(-u/M) \cong \hat{G}(0)\delta(u) - 2\{\hat{\varphi}(u)[G^i]^\wedge(u) + \hat{\mu}(u)[G^r]^\wedge(u)\}, \quad (15)$$

where $[G^r]^\wedge$ and $[G^i]^\wedge$ are respectively the amplitude and phase transfer functions and are expressed *via* the system transfer function as follows (Nesterets *et al.*, 2005):

$$[G^r]^\wedge(u) = \tfrac{1}{2}[\hat{G}(u,0) + \hat{G}^*(-u,0)],$$

$$[G^i]^\wedge(u) = \tfrac{1}{2i}[\hat{G}(u,0) - \hat{G}^*(-u,0)].$$

Equation (15) represents the 'weak-object' (WO) approximation and is linear with respect to the phase and amplitude of the object wave. The WO approximation is used below for solution of the phase-retrieval problem in ABI.

3. Numerical results and quantitative comparison of GO and WO approaches to ABI

3.1. Aberration-free optical system

The main problem that usually arises when implementing a reconstruction method is the assessment of the reconstruction error. This problem occurs due to the lack of prior information about an object whose transmission function is reconstructed using experimental data. As a result, a direct comparison of the reconstructed and actual parameters of the object becomes problematic. The problem can be resolved if
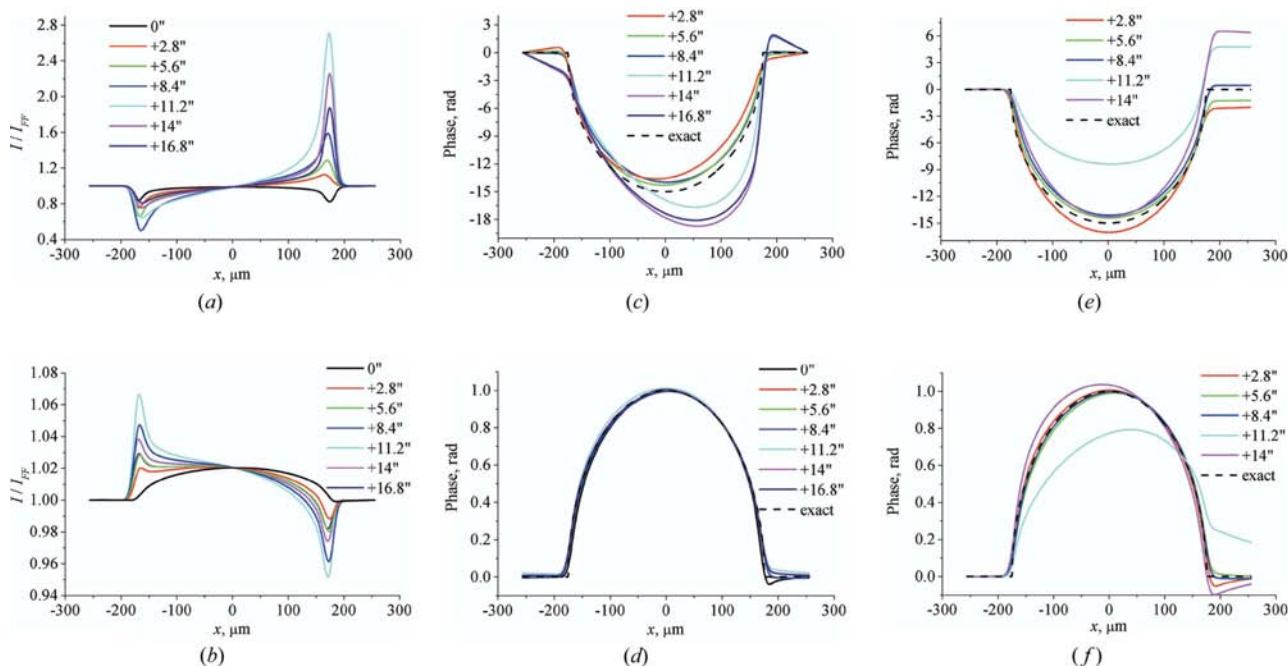

Figure 2
Intensity cross sections of the images of (*a*) a Nylon fibre of 350 µm diameter in vacuum, object 1, and of (*b*) a Perspex fibre of 350 µm diameter in water, object 2, calculated under the assumption of an incident quasimonochromatic plane wave at different angular deviations of the analyser. Symmetrical Si(111) reflections for all the crystals and σ-polarized X-radiation of average energy 25 keV were used in the calculations. Results of the phase reconstruction of object 1 and object 2 using the weak-object approximation, (*c*) and (*d*), respectively, and the geometrical optics approximation, (*e*) and (*f*), respectively.

numerically simulated images of a model object are used for testing of the reconstruction method.

We calculated intensity profiles for two cylindrical objects (object 1: nylon wire of 350 µm diameter and 0.93 g cm^{-3} density in vacuum; and object 2: perspex wire of 350 µm diameter and 1.19 g cm^{-3} density in water) for 13 positions of the analyser crystal with angular step 2.8 µrad. We assumed 25 keV average energy of the polychromatic source of X-rays and symmetrical 111 reflections in the double-crystal monochromator and single-crystal analyser in our calculations. At the chosen energy, the maximum phase shift and intensity attenuation due to the object were -15 rad and 1%, respectively, for object 1. For object 2, the maximum phase shift and intensity gain (negative attenuation compared to the equivalent propagation in water) were $+1$ rad and 2.02%, respectively. In order to model finite detector resolution, the calculated intensity profiles were convolved with a Gaussian distribution with standard deviation of 15 µm. The resultant intensity profiles for the zero and positive deviations of the analyser normalized to the corresponding flat fields are shown in Figs. 2(a) and 2(b) corresponding to object 1 and object 2, respectively.

First, the phase reconstruction algorithm developed by Nesterets *et al.* (2004) for a homogeneous object and based on the weak-object approximation was applied to the intensity profiles in Figs. 2(a) and 2(b) and the results of the reconstructions are presented in Figs. 2(c) and 2(d), respectively. We should emphasize that a single image recorded at an arbitrary deviation angle of the analyser is used in this algorithm. As can be seen in Fig. 2(c), the quality of the reconstruction of the phase of object 1 strongly depends on the analyser deviation angle. For example, for values of this angle of $+2.8$, $+5.6$ and $+8.4$ µrad, the quality of the reconstruction is quite satisfactory although there is a small asymmetry in the profiles of the reconstructed phase and the maximum phase shifts are smaller than the exact value. For larger deviation angles, the reconstructed phase profiles reveal strong asymmetry and the maximum phase shifts are overestimated. For object 2 whose transmission function is characterized by a much smaller maximum phase shift (although the same geometrical parameters), the quality of the phase reconstruction is quite good and is almost independent of the analyser deviation angle (see Fig. 2d).

The results of the phase reconstruction using an algorithm based on equation (10) (note that we consider a pure analyser-based imaging in this section and the absorption is weak) are presented in Figs. 2(e) and 2(f). Considering Fig. 2(e), we should mention that, similarly to the case of the reconstruction using the weak-object approach, the quality of the GO phase reconstruction also strongly depends on the analyser deviation angle and the tendency is the same as in the former case. However, the phase profiles look different compared to those in Fig. 2(c). In the case of object 2 (see Fig. 2f), the reconstructed phase profiles corresponding to deviation angles of $+2.8$, $+5.6$ and $+8.4$ µrad almost coincide with the exact profile used for the simulations of the ABI intensity profiles. However, for the deviation angle $+11.2$ µrad, the result of the

phase reconstruction differs significantly from the exact phase. For the larger deviation angle, $+14$ µrad, the result of the phase reconstruction is much better although it is still worse compared to the results corresponding to the first three angles.

The behaviour of the phase reconstruction quality in the GO approximation can be understood from the comparison of the values of the left-hand side (l.h.s.) of equation (11) corresponding to the two objects and different deviation angles of the analyser.

In order to evaluate the l.h.s. of equation (11) for the cylindrical object, the following considerations were taken into account. We used a 0.5 µm step in the sampling of the object transmission function in our simulations. This finite sampling imposes certain limitations on the first and second derivatives of the object transmission function q. For simplicity, we restrict our analysis to the case of a pure phase object. In this case, we can present the transmission function derivatives in equation (11) as follows:

$$[q'(x)/q(x)]^2 = -[\varphi'(x)]^2 \text{ and } q''(x)/q(x) = i\varphi''(x) - [\varphi'(x)]^2.$$

The maxima of the first and second derivatives of the phase function are expected at the edges of the cylinder where the phase can be approximated by the following expression:

$$\varphi(\Delta x) \cong \begin{cases} \varphi_0\sqrt{2\dfrac{\Delta x}{R}}, & 0 \le \Delta x \ll R, \\ 0, & \Delta x < 0. \end{cases}$$

Here Δx is the distance from the edge towards the centre of the cylinder, R is the radius of the cylinder and φ_0 is the maximum phase shift due to the cylinder. At the left edge of the cylinder, the first and second derivatives of the phase take the following form:

$$\varphi'(x) = \varphi'(\Delta x) \cong \begin{cases} \dfrac{\varphi_0}{2\Delta x}\left(2\dfrac{\Delta x}{R}\right)^{1/2}, & 0 \le \Delta x \ll R, \\ 0, & \Delta x < 0. \end{cases}$$

$$\varphi''(x) = \varphi''(\Delta x) \cong \begin{cases} -\dfrac{\varphi_0}{4(\Delta x)^2}\left(2\dfrac{\Delta x}{R}\right)^{1/2}, & 0 \le \Delta x \ll R, \\ 0, & \Delta x < 0. \end{cases}$$

The maximum increase of the phase on the length of the sampling step h is $\Delta\varphi_{max} = \varphi(h) = \varphi_0(2h/R)^{1/2}$. The corresponding maximum values of the first and second derivatives are $\varphi'_{max} = \varphi'(h) = \Delta\varphi_{max}/(2h)$ and $\varphi''_{max} = \varphi''(h) = -\Delta\varphi_{max}/(2h)^2$.

Numerical values for the derivatives of the object transmission function for both test objects are summarized in Table 1. Table 2 contains information on the transfer-function derivatives and the corresponding numerical values of the l.h.s. of equation (11) for object 1 and object 2 for different deviations of the analyser crystal. We should emphasize here that the only difference between the two objects is the maximum phase shift φ_0. All other parameters are the same.

3.2. Effect of the incident wavefront curvature

So far we have considered the case of a plane wavefront incident on the object. In a real experiment, this wavefront is

Table 1
Characteristics of the objects used in the numerical simulations.

	φ_0 (rad)	$\Delta\varphi_{\max}$ (rad)	max $|q'/q|^2$ (μm^{-2})	max $|q''/q|$ (μm^{-2})
Object 1	-15	-1.14	1.30	1.73
Object 2	$+1$	0.076	0.0058	0.076

Table 2
Values of the transfer-function derivatives and the corresponding values of the l.h.s. of equation (11).

ω_3 (μrad)	$|\partial^2_{UU}\hat{G}/\hat{G}|$ (μm^2)	$|\partial^2_{UV}\hat{G}/\hat{G}|$ (μm^2)	Object 1	Object 2
0	0.27×10^3	0.15×10^3	0.08	1.9
2.8	0.15×10^3	0.13×10^3	0.15	3.3
5.6	0.17×10^3	0.14×10^3	0.14	3.1
8.4	0.20×10^3	0.17×10^3	0.11	2.5
11.2	0.30×10^3	0.24×10^3	0.07	1.7
14.0	0.11×10^3	0.10×10^3	0.20	4.5

usually non-flat. We should emphasize that this non-flatness is in general different from the spherical wavefront assumed for each monochromatic wave radiated by a point source (see §2.1). The latter was effectively taken into account by means of the appropriate choice of the transfer functions in equation (3). Moreover, integration of the image intensity over the wavelength resulted in the general equation (4) in which the sphericity of the wave radiated by a point source leads to the appearance of the additional terms in the arguments of the amplitude reflection coefficients in equation (6). These terms are explicitly described by magnification M which characterizes quantitatively the sphericity of the incident wavefront.

Another source of non-flatness of the wavefront of the wave incident on the object is related to the imperfections of the imaging system. These imperfections may include the non-uniformity and thickness variations of various optical elements in the imaging system as well as possible curvature of the crystals in the monochromator and analyser which are assumed to be flat (in the following, we assume that the detector is perfect, in the sense that it does not introduce wavefront aberrations). As we have already mentioned in the *Introduction*, this type of wavefront curvature cannot be corrected for by a simple division of the images of the object by the corresponding flat-field images. This can only compensate the transverse non-uniformity of the intensity in the wave incident on the object but not the wavefront curvature. The curvature results in the different local deviation angles of the analyser crystal at different points in the image. The spread of these angles is defined by the curvature of the wavefront and the field of view and can be large. This fact complicates significantly the phase reconstruction using both the weak-object and geometrical optics approximations.

The main difficulty with the weak-object approximation is that the optical system can no longer be considered as shift invariant and this results in the failure of the main expression of this approximation, equation (15). In the case of a slowly varying 'aberration' phase φ_0 in the incident wave (so that the geometrical optics approximation is valid for the incident wave), we can express the intensity distribution in the image $I(x, y; \omega)$ formed by a non-flat incident wave *via* the corresponding image $I_{\mathrm{pl}}(x, y; \omega)$ corresponding to the plane incident wave as follows:

$$I(x, y; \omega) \cong I_{\mathrm{pl}}(x, y; \omega + k^{-1}\partial_x\varphi_0(x, y)), \qquad (16)$$

where ω is the analyser deviation angle defined for the plane incident wave. Equation (15) is valid for the intensity $I_{\mathrm{pl}}(x, y; \omega)$ but is invalid for the intensity $I(x, y; \omega)$. At least two

approaches can be suggested in order to overcome this problem.

First, if the phase φ_0 of the incident wave is known *a priori* and the range of deflection angles $\theta = k^{-1}\partial_x\varphi_0$ in the incident wave is small compared to the analyser's rocking-curve width (slowly varying phase φ_0 and/or small field of view), then the following approach can be used. Equation (16) can be presented as

$$I_{\mathrm{pl}}(x, y; \omega) \cong I(x, y; \omega) - \theta(x, y)\partial_\omega I_{\mathrm{pl}}(x, y; \omega). \qquad (17)$$

Given only one image of an object (one image is enough for reconstruction of the phase of a homogeneous object), equation (17) can be solved iteratively. At the first iteration, the second term on the right-hand side (r.h.s.) is neglected and the zeroth approximation for the object's phase is found. Using this phase, the intensity derivative is calculated numerically and thus a correction [the second term on the r.h.s. of equation (17)] for the non-flatness is found. At the second iteration, the corrected image is used for the phase reconstruction. The iterative procedure is stopped when convergence of the phase is achieved.

The second approach is based on a series of images for the analyser deviation angles covering the total range of incident-wave deflection angles. The phase of the incident wave is assumed to be known. Equation (16) can be rewritten in the alternative form

$$I_{\mathrm{pl}}(x, y; \omega) \cong I(x, y; \omega - k^{-1}\partial_x\varphi_0(x, y)). \qquad (18)$$

Using an appropriate interpolation algorithm, the image corresponding to the plane incident wave is first reconstructed. This image is then used for the phase reconstruction based on equation (15).

Strictly speaking, the validity of both suggested approaches depends not only on the slowness of the phase of the incident wave but also on the object under investigation. The smoothness of the image intensity as a function of the analyser deviation angle was implicitly assumed in both approaches. This in its turn imposes some (unknown) restrictions on the object transmission function and the transfer function of the system.

We now turn our attention to the same problem in the geometrical optics approximation. The main difficulty in the application of this approach to the phase reconstruction is a possible non-uniqueness of the solution. The latter arises in the case when both sides of the analyser's rocking curve

contribute to the formation of the image. Then some additional assumptions about the phase induced by the object are to be made (for example, phase derivative continuity, boundary conditions *etc.*) in order to perform the phase/amplitude reconstruction. To avoid the non-uniqueness problem, an appropriate working point at one of the rocking-curve slopes is usually chosen, such that only one slope of the rocking curve contributes to the formation of the whole image. This condition can be strongly violated in the case of a non-flat wavefront of the incident wave. Then, for some points in the image, both slopes of the rocking curve could contribute. Thus, the non-uniqueness problem mentioned above arises again. In the real experiment, one does not know *a priori* whether or not the 'one-slope' condition is fulfilled. Below, we present an alternative approach to the phase reconstruction based on the geometrical optics approximation which guarantees the uniqueness of the phase reconstruction and resolves the incident non-flatness problem.

4. Multi-image approach to the ABI

An alternative approach to the phase reconstruction in ABI is considered below. It is based on the geometrical optics approximation and consists of measuring a series of images corresponding to different deviations of the analyser crystal. It should be mentioned here that the relative positions of the analyser crystal rather than absolute positions are assumed to be known. Therefore, the offset of the analyser deviation is arbitrary, but the angular distances between the analyser positions have to be precisely measured.

Let θ_i designate the analyser deviation for the ith measurement in the series of N measurements. The corre-

sponding images in the presence of the object and in its absence are denoted by $I_i(x, y)$ and $I_i^{FF}(x, y)$, respectively. If the validity conditions of the geometrical optics approximation are satisfied, then the angular dependence of the intensity at an arbitrary point of the image should reproduce the rocking curve of the analyser crystal. Owing to the non-flatness of the wavefront incident on the analyser, the angular distributions corresponding to different points in the image are shifted with respect to each other. These shifts contain information about the phase derivative of the wave incident on the analyser and allow one to reconstruct the phase derivative and, given the boundary conditions, the phase itself.

In order to extract the qualitative information about phase and intensity distribution in the wave incident on the analyser crystal, we approximate the angular distribution for each point in the image with some function using a least-squares minimization procedure. In the following, we use a Gaussian distribution, which is a good choice for approximation of typical experimental rocking curves,

$$I(\theta; x, y) = c(x, y) + A(x, y) \exp\{-[\theta - \theta_c(x, y)]^2/[2w^2(x, y)]\}. \quad (19)$$

The inclusion of the offset $c(x, y)$ allows better modelling of the rocking curves at their tails. Given the maps of the coefficients of the approximating function (19) as functions of the (x, y) position in the images with and without the object, the following distributions are then calculated.

1. 'Average absorption', defined as the ratio

$$\langle I \rangle(x, y) / \langle I^{FF} \rangle(x, y)$$
$$= \{c(x, y) + (2\pi)^{1/2} w(x, y) A(x, y)\}$$
$$\times \{c^{FF}(x, y) + (2\pi)^{1/2} w^{FF}(x, y) A^{FF}(x, y)\}^{-1}$$
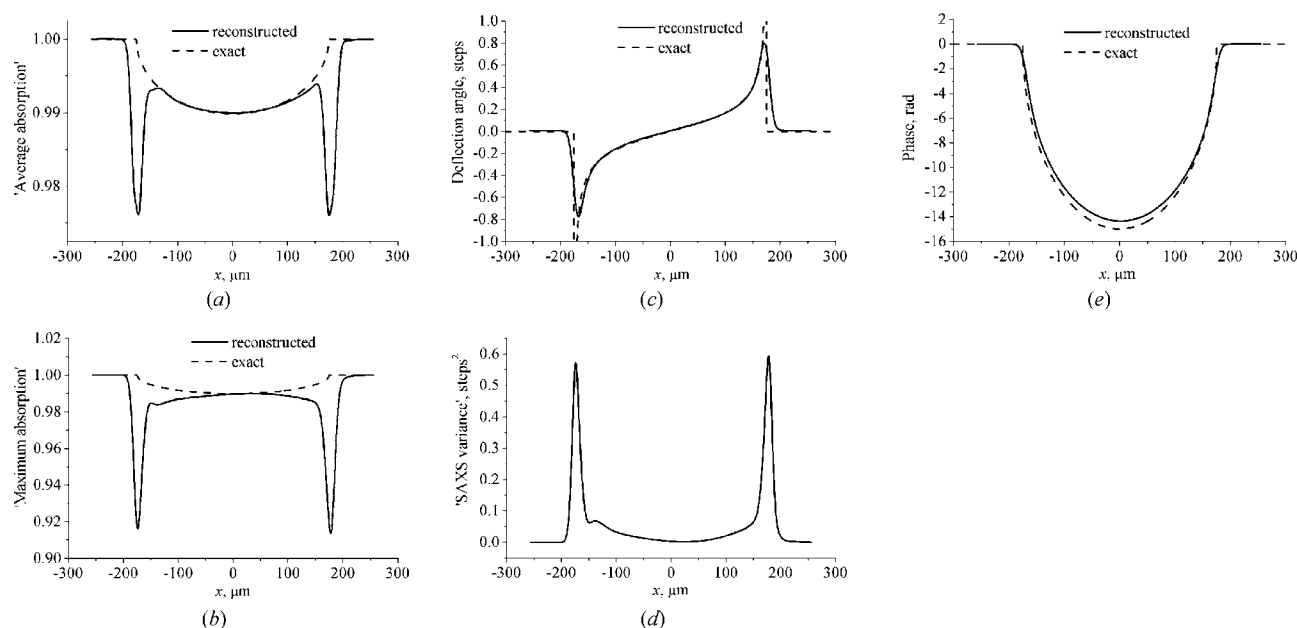

Figure 3
(*a*)–(*d*) Cross sections of four parametric images of object 1 calculated using the multi-image approach to the simulated images presented in Fig. 2(*a*). (*e*) Cross section of the phase map obtained by integration of the 'deflection angle' map presented in (*c*).

2. Refraction angle, defined as the difference $\theta_c(x, y) - \theta_c^{FF}(x, y)$.

3. 'Maximum absorption', defined as the ratio

$$I_c(x, y)/I_c^{FF}(x, y) = \{c(x, y) + A(x, y)\}/\{c^{FF}(x, y) + A^{FF}(x, y)\}.$$

4. 'Small-angle-scattering variance', defined as the difference $w^2(x, y) - (w^{FF})^2(x, y)$.

4.1. Phase reconstruction using the multi-image approach. Simulated data

We have calculated four maps ('average absorption', 'maximum absorption', 'deflection angle' and 'SAXS variance') for the simulated images (see §3) using the multi-image approach, equation (19). The results for object 1 are presented in Figs. 3(a)–(d). By numerical integration of the 'deflection-angle' distribution, the corresponding phase distribution has been reconstructed. This is shown in Fig. 3(e). Analysis of Fig. 3(a), where the solid line represents the 'average-absorption' distribution and the dashed line represents the exact intensity attenuation due to the object, shows that the multi-image approach based on the Gaussian approximation of the local rocking curves gives accurate reconstruction of the attenuation function except for the cylinder edges. Near the edges, the reconstruction gives anomalously large attenuation (intensity gaps). These gaps are sometimes interpreted as the result of 'extinction' contrast in the images due to small-angle scattering. In fact, the actual source of these gaps in the reconstructed intensity is in the violation of the geometrical optics approximation (as well as the weak-object approximation, or any other approximation, such as e.g. DEI, which is based on the GO or WO approximations) in the vicinity of edges of cylindrical objects (and in any other regions with a rapid change of the projected

refractive index). Therefore, the use of any technique based on the GO or the WO approximation for quantitative interpretation of these intensity gaps cannot be justified.

Fig. 3(b) shows the 'maximum-absorption' contrast. In theory, it should provide the pure absorption contrast due to the object. However, strong artefacts are clearly seen in the figure and the reconstructed profile disagrees significantly with the exact absorption profile. We attribute this behaviour to the local failure of the geometrical optics approximation for the object under investigation.

Fig. 3(c) presents the deflection angle profile together with the exact one. We have integrated this profile in order to obtain the phase distribution (Fig. 3e). Analysis of the phase profile shows that the multi-image approach gives a satisfactory result but slightly disagrees with the exact phase profile. We relate this discrepancy to the failure of the geometrical optics approximation for the object.

The local rocking-curve broadening shown in Fig. 3(d) is usually related to the small-angle scattering at very small features of the object. We used a cylinder with a smooth surface in our calculations and we did not take into account any small angular scattering in our simulations. We attribute the broadening of the local rocking curves to the failure of the geometrical optics approximation.

In order to prove our hypothesis (the failure of the geometrical optics approximation for the considered object) about the origin of the strong artefacts in the calculated maps of 'average' and 'maximum' intensities and rocking-curve broadening, we performed the same calculations for object 2. The corresponding cross sections of the four parametric images of the object are shown in Figs. 4(a)–(d). Fig. 4(e) presents the reconstructed phase profile together with the exact one. The 'average' absorption distribution reproduces the exact profile with high accuracy. The same is true for the
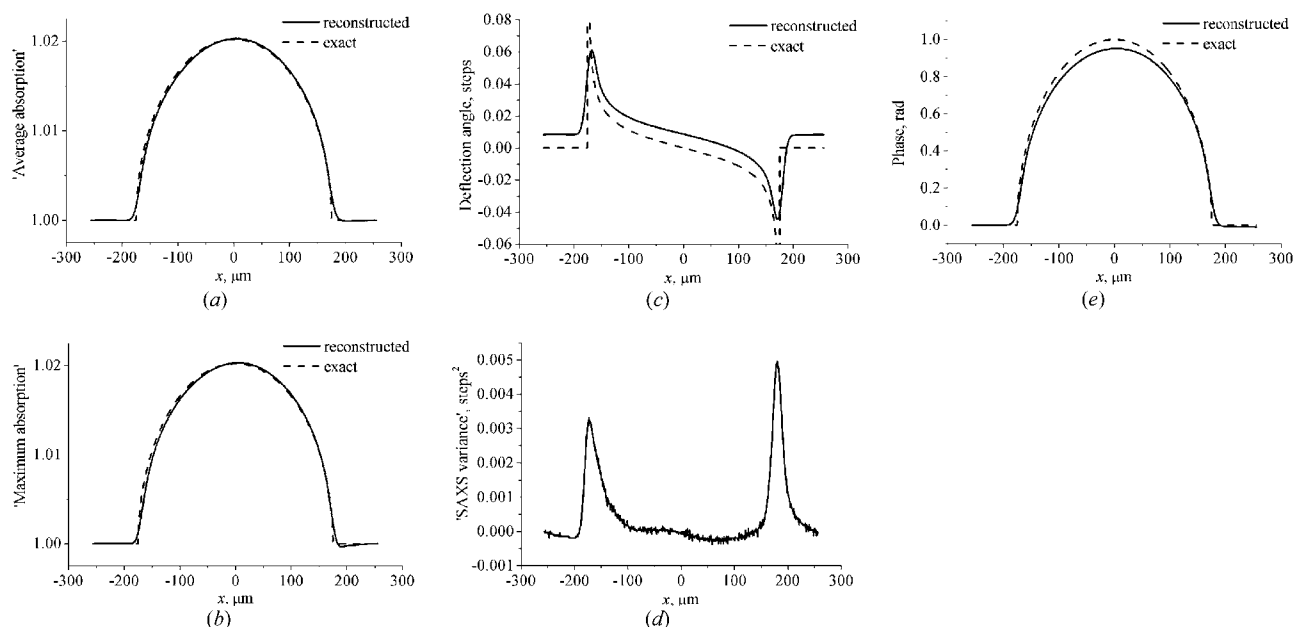

Figure 4
Same as in Fig. 3 but for object 2.

Table 3
Chemical formulae and densities of the materials of the fibres.

Material	Chemical formula	Density (g cm^{-3})
Nylon	$C_{12}H_{22}N_2O_2$	1.14
PTFE	C_2F_4	2.13
Kevlar	$C_{14}H_{10}N_2O_2$	1.44

Table 4
Optical parameters (real and imaginary parts of the refractive-index decrement, δ and β, respectively, the linear phase shift and the linear attenuation coefficient, φ and μ, respectively, referred to vacuum) at the X-ray energy 25 keV for the fibre materials used in the experiment.

Material	δ	β	φ (mm^{-1})	μ (cm^{-1})	δ/β
Nylon	0.4148×10^{-6}	1.4089×10^{-10}	-52.55	0.357	2944
PTFE	0.6792×10^{-6}	4.2187×10^{-10}	-86.05	1.069	1610
Kevlar	0.4977×10^{-6}	1.7404×10^{-10}	-63.06	0.441	2860

'maximum' absorption distribution. The latter is in excellent agreement with the exact profile. The 'SAXS variance' profile shown in Fig. 4(d) has peaks at the edges of the cylinder. However, these are two orders of magnitude smaller compared to the values obtained for object 1. The reconstructed phase profile reproduces the shape of the exact phase distribution although the magnitude of the reconstructed profile is smaller than that of the exact one.

## 4.2. Application of the multi-image approach to the experimental images

The experiment was performed at the ID19 beamline of the European Synchrotron Radiation Facility (ESRF, Grenoble, France) and the schematic diagram of the experimental set-up is presented in Fig. 1. The X-ray source used was an 11-pole variable-field wiggler with tunable photon energy 6–100 keV. The source-to-object distance was about 145 m and object-to-detector distance was 0.2 m. A fixed-exit double-crystal Si(111) monochromator and single-crystal Si(111) analyser were both operating in symmetric Bragg geometry in the vertical plane. The experimental data were acquired using 25 keV X-rays. The measured analyser rocking-curve width (FWHM) was 14.5 μrad and the angular interval between the analyser positions was 2.8 μrad. More details of the experiment can be found in Coan et al. (2005).

We have applied the weak-object approximation and the multi-image approach to the experimental images of the set of four fibres together with the corresponding flat-field images collected at 13 equidistant deviation angles of the analyser. The parameters of the fibres are given below:
  – nylon fibre: diameter = 350 μm;
  – PTFE (Teflon) fibre: diameter = 260 μm;
  – kevlar fibre: diameter = 100 μm;
  – kevlar fibre: diameter = 16.7 μm.
The chemical formulae and densities of the materials of the fibres and their optical properties at the X-ray energy 25 keV are given in Table 3 and Table 4, respectively.

The first problem that arises immediately in the processing of the raw experimental images is the non-uniformity (curvature) of the wavefront incident on the object. This results in the appearance of artefacts in the images normalized by the corresponding flat-field images. As an example, Figs. 5(a), (c), (e) present three normalized experimental images corresponding to deviation angles of the analyser of -2.8, 0 and $+2.8$ μrad. One such artefact is the broad strip clearly visible in Fig. 5(c) and 5(e). Moreover, the contrast in each image changes slowly with position in the image in both directions. This can be explained by the fact that even in the absence of an object the non-uniformity of the incident wavefront results in different angles of incidence of X-rays at different points of the analyser, i.e. the local deviation angle of the analyser which defines the contrast is not constant but slowly varying along the analyser surface.
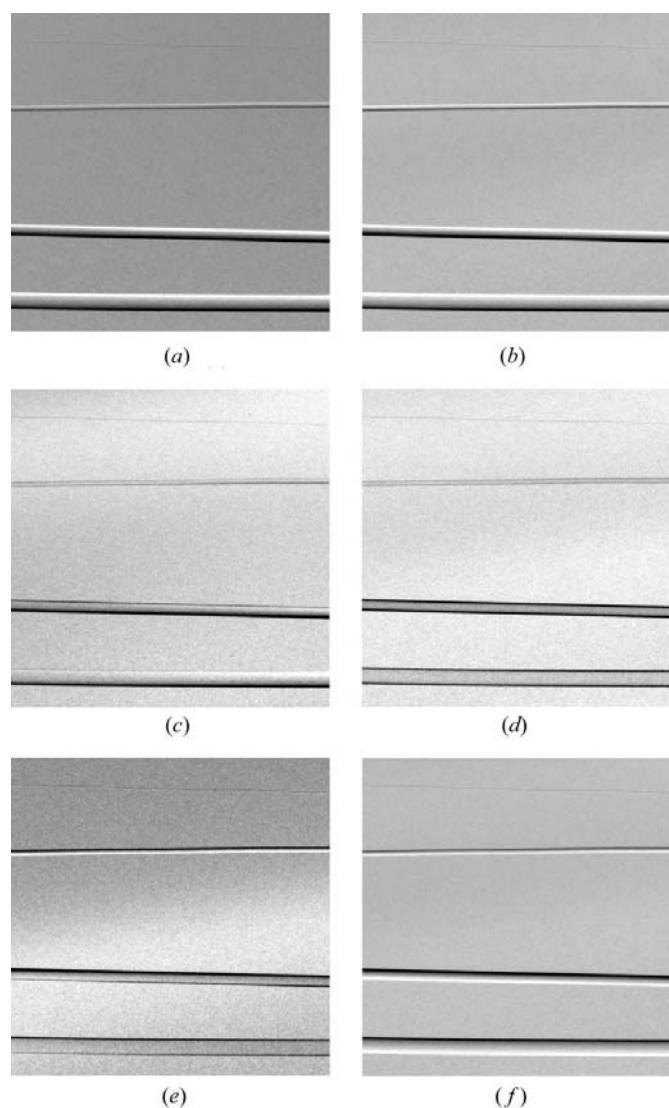
Figure 5
Normalized experimental images of a set of fibres for three deviation angles of the analyser: -2.8 μrad (a) and (b), 0 μrad (c) and (d), and $+2.8$ μrad (e) and (f); before (a), (c), (e) and after (b), (d), (f) the correction for the incident wavefront non-uniformity.

We have already pointed out that the phase reconstruction algorithm based on the weak-object approximation cannot be directly applied to such images and the correction of the images for the incident wavefront curvature is needed. Two methods for such a correction have been described in §3. Here we applied the second approach based on interpolation of the local angular intensity distributions of the images with and without objects using a Gaussian function, equation (19). First, we obtained the maps of eight interpolation coefficients using 13 images with objects and 13 flat-field images. These maps have the same size, 1024 by 1024 pixels, as the original images. Using these maps, we then synthesized 13 images of the objects and 13 flat-field images corresponding to 13 values of the deviation angle θ of the analyser in each pixel, namely, $\pm16.8, \pm14.0, \pm11.2, \pm8.4, \pm5.6, \pm2.8$ and 0 µrad. Given these images, we calculated 13 normalized images of the objects. Three of them, for ±2.8 and 0 µrad deviations of the analyser, are presented in Figs. 5(b), (d), (f). All these images are free from the artefacts observed in the original images and, unlike the latter, have uniform contrast over the whole field of view.

As the sample consists of fibres of different materials, it cannot be treated as a homogeneous object (δ/β ratios are different for different materials, see Table 4). We have implemented a WO-based algorithm described in our earlier paper (Nesterets et al., 2004). It requires two images collected at different deviation angles of the analyser in order to reconstruct both phase φ and attenuation function μ of the object transmission function q. We applied this algorithm to three pairs of images corresponding respectively to $\pm2.8, \pm5.6$ and ±8.4 µrad. The results of the reconstructions are presented in Fig. 6. Analysis of the phase and attenuation profiles shows that these are different for different pairs of images. The maximum phase values for each of the four fibres differ significantly, see Fig. 6(a). For example, the maximum of the reconstructed phase of the Nylon fibre (the leftmost one in Fig. 6) is about -15.5 rad for the reconstruction using ±2.8 µrad images, -20 rad for ±5.6 µrad images and -15 rad for ±8.4 µrad images. For comparison, according to Table 4, the expected theoretical value of the maximum phase shift for a Nylon fibre of 350 µm diameter at 25 keV is approximately -18.4 rad. Such a large difference in the reconstructed phase values was observed earlier in §3 using numerically simulated images. This is an explicit indication that the validity conditions of the weak-object approximation are violated for the objects under investigation. Analysis of Fig. 6(b) gives us another confirmation of this conclusion. Indeed, the attenuation function exhibits strong artefacts near the edges of the fibres. Moreover, these artefacts have different signs for different reconstructions.

Finally, we have applied the multi-image approach to the experimental images. We used the maps of parameters of the Gaussian interpolation function, equation (19), and calculated four maps as described at the beginning of this section. The results of the reconstruction are presented in Fig. 7. Fig. 7(a) shows the 'average-absorption' image of the fibres. The 'maximum-absorption' image in Fig. 7(b) contains strong 'edge' artefacts and this implicitly indicates that the validity
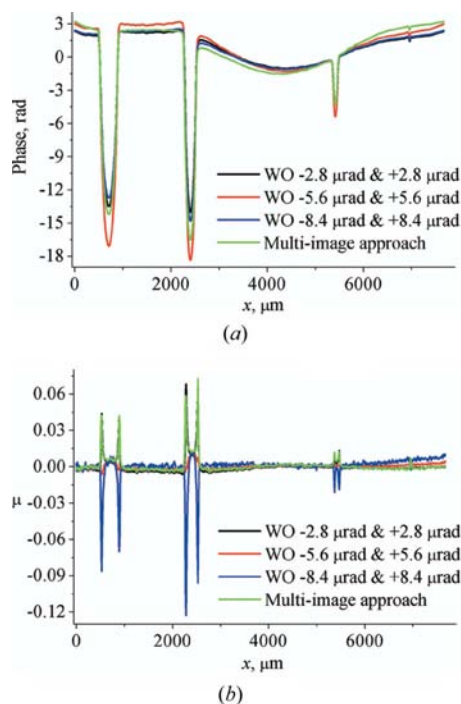

Figure 6
Results of the phase and attenuation function reconstruction for the set of four fibres using the weak-object approximation applied to the pairs of experimental images: ±2.8 µrad (black), ±5.6 µrad (red) and ±8.4 µrad (blue). Green lines represent the results of reconstruction using the multi-image approach applied to the total set of 13 experimental images of the object and 13 flat-field images.
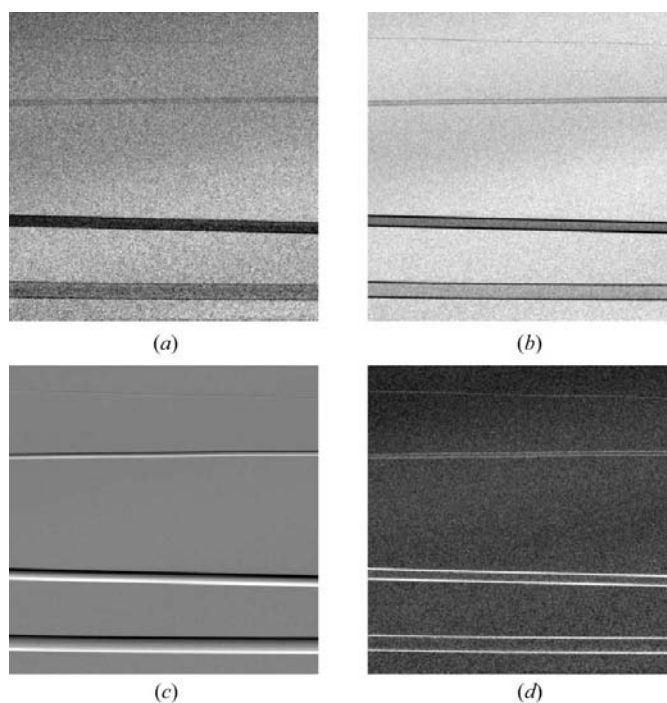

Figure 7
Parametric images of the set of four fibres calculated using the multi-image approach applied to the total set of 13 experimental images of the object and 13 flat-field images.

conditions for the objects under investigation are violated. A cross section of the corresponding distribution of the attenuation function μ is shown in Fig. 6(b). The deflection angle map, Fig. 7(c), looks very smooth and it does not contain noise and artefacts characteristic to the raw images. A cross section of the phase map obtained by proper integration of the deflection angle map is also shown in Fig. 6(a). Finally, the 'SAXS' map in Fig. 7(d) reveals strong peaks at the edges of the fibres.

These results confirm that the use of the proposed multi-image approach allows one to successfully compensate for the effect of incident wavefront curvature. However, the violation of the validity conditions of the geometrical optics and the weak-object approximations cannot be overcome within the considered approach. As follows from Fig. 7, the reconstructed average and maximum absorption maps as well as the rocking-curve-broadening map contain artefacts near the edges of the cylinders. This fact and the results of our numerical simulations and reconstructions presented in §§3 and 4.1 allow us to conclude that the objects under investigation do not satisfy the validity conditions of the geometrical optics approximation. Thus the reconstructed phase distribution has qualitative rather than quantitative character. Unlike the simulated images, the error of the reconstructions cannot be estimated for the experimental data. However, comparison of the reconstructed phase with the phase calculated using the theoretical values for the optical constants and diameters of the cylinders allows us to conclude that the reconstructed phase is smaller than the theoretical one. This is in agreement with the results obtained in §4.1 for simulated images.

5. Conclusions

We have performed a detailed analysis of the theoretical and practical aspects of analyser-based phase-contrast imaging. The main outcomes of this analysis can be briefly summarized as follows.

The theoretical base for the phase/amplitude reconstruction has been re-examined and extended. In particular, using rigorous wave-optical formalism, a general expression, equations (4)–(6), for the intensity in the image formed in the combined analyser-based/propagation-based phase-contrast imaging has been derived. Unlike the previous theoretical considerations in Pavlov *et al.* (2004) and elsewhere which assumed a monochromatic plane incident wave, the results of this paper describe an image formation in the case of partially coherent radiation incident on the object.

In order to solve the corresponding inverse problem of complex object wave reconstruction, the general expression (4) for the intensity distribution in the image has to be inverted with respect to the object transmission function. In general, such a solution is quite problematic unless the non-linear integral equation (4) is simplified. Two approaches leading to significant simplification of equation (4) and allowing its inversion with respect to the object transmission function have been considered in this paper. The first approach is the new quasi-monochromatic form of the

geometrical optics approximation for ABI, which is based on the linearization of the transfer function of the imaging system resulting in equation (9) in the case of a quasi-monochromatic plane X-ray wave incident on the object and a perfect detector. Validity condition (11) of the geometrical optics approximation has been formulated which imposes simultaneous restrictions on the curvature of the transfer function of the imaging system and on the smoothness of the transmission function of the object. The second approach, the so-called weak-object approximation, consists of linearization of the object transmission function. It was investigated earlier by Nesterets *et al.* (2005) and follows immediately from the general expression (4) of this paper if the appropriate conditions on the phase and attenuation induced by the object are satisfied. The violation of the formulated validity conditions of the geometrical optics or the weak-object approximations leads to the appearance of artefacts in the reconstructed distributions of the phase and amplitude of the object wave. In practice, such artefacts are usually most noticeable near the edges of strongly scattering objects, where the projected X-ray refractive index changes rapidly as a function of transverse position. Such artefacts are sometimes incorrectly attributed to small-angle scattering.

Another problem arising due to the imperfections of the imaging system, namely the non-uniformity of the wavefront of the incident wave, has been investigated in this paper. Unlike the non-uniformity of the incident-intensity distribution, this wavefront non-uniformity cannot be compensated for by normalization of the images of the objects with the help of the corresponding flat-field images, and results in additional difficulties in the solution of the phase/amplitude reconstruction problem. A method for correction of the images for the non-uniformity of the incident wavefront has been developed. It is based on the geometrical optics approximation and consists in measuring a series of images corresponding to a sufficiently wide range of analyser deviation angles spanning the whole reflectivity curve. This multi-image approach allows one to obtain parametric maps of the object properties such as 'average absorption', 'maximum absorption', 'deflection angle' and 'small-angle-scattering variance' and thus solves the phase/amplitude reconstruction problem.

The developed approaches (WO, GO and multi-image approaches) have been applied to the reconstruction of the simulated as well as the experimental images of fibre objects. In agreement with the preceding theoretical analysis, it was shown that, if the validity conditions of the geometrical optics or weak-object approximation are not satisfied, strong artefacts appear near the edges of the objects in the intensity distributions obtained by using reconstruction algorithms based on either approximation and the results of the reconstruction of the phase and amplitude are in general qualitatively incorrect. Within the image regions where the relevant validity conditions were satisfied, the developed methods allowed us to successfully compensate for the curvature of the incident wavefront and reconstruct the desired maps of the object properties which were free from the artefacts induced by the aberrations of the incident wavefront.

References

Bushuev, V. A., Ingal, V. N. & Beliaevskaya, E. A. (1996). *Crystallogr. Rep.* **41**, 766–774.

Bushuev, V. A., Ingal, V. N. & Beliaevskaya, E. A. (1998). *Crystallogr. Rep.* **43**, 538–547.

Bushuev, V. A., Ingal, V. N., Beliaevskaya, E. A. & Sergeev, A. A. (2002). *Metallofiz. Nov. Tekhnol./Met. Phys. Adv. Tech.* **24**, 559–569.

Bushuev, V. A. & Sergeev, A. A. (1999). *Tech. Phys. Lett.* **25**, 83–85.

Chapman, D., Thomlinson, W., Johnston, R. E., Washburn, D., Pisano, E., Gmur, N., Zhong, Z., Menk, R., Arfelli, F. & Sayers, D. (1997). *Phys. Med. Biol.* **42**, 2015–2025.

Coan, P., Pagot, E., Fiedler, S., Cloetens, P., Baruchel, J. & Bravin, A. (2005). *J. Synchrotron Rad.* **12**, 241–245.

Davis, T. J., Gao, D., Gureyev, T. E., Stevenson, A. W. & Wilkins, S. W. (1995*a*). *Nature (London)*, **373**, 595–598.

Davis, T. J., Gao, D., Gureyev, T. E., Stevenson, A. W. & Wilkins S. W. (1995*b*). *Phys. Rev. Lett.* **74**, 3173–3176.

Fitzgerald, R. (2000). *Phys. Today*, **53**, 23–26.

Förster, E., Goetz, K. & Zaumseil, P. (1980). *Krist. Tech.* **15**, 937–945.

Gureyev, T. E. & Wilkins, S. W. (1997). *Nuovo Cim. D*, **19**, 545–552.

Indenbom, V. L. & Chukhovskii, F. N. (1972). *Sov. Phys. Crystallogr.* **16**, 972–978.

Ingal, V. N. & Beliaevskaya, E. A. (1995). *J. Phys. D*, **28**, 2314–2317.

Ingal, V. N., Beliaevskaya, E. A. & Efanov, V. P. (1994). RU Patent No. 2012872.

Ingal, V. N., Beliaevskaya, E. A. & Efanov, V. P. (1995). US Patent No. 5579363.

Nesterets, Ya. I., Gureyev, T. E., Paganin, D., Pavlov, K. M. & Wilkins, S. W. (2004). *J. Phys. D*, **37**, 1262–1274.

Nesterets, Ya. I., Gureyev, T. E. & Wilkins, S. W. (2005). *J. Phys. D*, **38**, 4259–4271.

Oltulu, O., Zhong, Z., Hashah, M., Wernick, M. N. & Chapman, D. (2003). *J. Phys. D*, **36**, 2152–2156.

Pagot, E., Cloetens, P., Fiedler, S., Bravin, A., Coan, P., Baruchel, J., Hartwig, J. & Thomlinson, W. (2003). *Appl. Phys. Lett.* **82**, 3421–3423.

Pavlov, K. M., Gureyev, T. E., Paganin, D., Nesterets, Ya. I., Morgan, M. J. & Lewis, R. A. (2004). *J. Phys. D*, **37**, 2746–2750.

Pinsker, Z. G. (1978). *Dynamical Scattering of X-rays in Crystals.* Berlin: Springer.

Rigon, L., Besch, H.-J., Arfelli, F., Menk, R.-H., Heitner, G. & Plothow-Besch, H. (2003). *J. Phys. D*, **36**, A107–A112.

Somenkov, V. A., Tkalich, A. K. & Shilstein, S. S. (1991). *J. Tech. Phys.* **61**, 197–201.

Wernick, M. N., Wirjadi, O., Chapman, D., Zhong, Z., Galatsanos, N. P., Yang, Y., Brankov, J. G., Oltulu, O., Anastasio, M. A. & Muehleman, C. (2003). *Phys. Med. Biol.* **48**, 3875–3895.